

Performance Evaluation for Retrieving Aerosol Optical Depth from Directional Polarimetric Camera (DPC) based on GRASP Algorithm

Shikuan Jin ¹, Yingying Ma ^{1,2,*}, Cheng Chen ^{4,5}, Oleg Dubovik ⁵, Jin Hong ⁶, Boming Liu ¹, Wei Gong ^{2,3}

¹ State Key Laboratory of Information Engineering in Surveying, Mapping and Remote Sensing, Wuhan University, China.

² Collaborative Innovation Center for Geospatial Technology, Wuhan 430079, China.

³ School of Electronic Information, Wuhan University, China.

⁴ GRASP-SAS, Remote Sensing Developments, Cite Scientifique, 59655 Villeneuve d'Ascq, France.

⁵ Univ. Lille, CNRS, UMR 8518 - LOA - Laboratoire d'Optique Atmosphérique, Lille, France.

⁶ Anhui Institute of Optics and Fine Mechanics, Chinese Academy of Sciences, Hefei 230031, China.

Corresponding Author: Yingying Ma (yym863@whu.edu.cn)

Abstract

Aerosol spatial distribution obtained from satellite sensors is critical for understanding regional aerosol environments, anthropogenic aerosol emissions, and global climate change. Directional Polarimetric Camera (DPC) is the first generation of multi-angle polarized sensor developed by China. It is onboard GaoFen-5 satellite, running in 705 km sun-synchronous orbit with a 13:30 pm ascending node. The sensor has three polarized channels at 490, 670, and 865 nm and ~9 viewing angles, mainly used for observing aerosols. The spatial resolution is ~ 3.3 km at nadir and global coverage is ~2 days. In this study, the performance of aerosol optical depth (AOD) retrievals from the DPC/GaoFen-5 using the Generalized Retrieval of Atmosphere and Surface Properties (GRASP) algorithm were evaluated on a global basis for the first time. The results showed that the DPC GRASP/Models scheme, which used several aerosol-type mixings, achieved good performance. By comparing with AERONET observations, the correlation coefficient (R), root mean square error, and Expected Error (EE%, $\pm(0.05+0.15*AOD)$) were 0.9007, 0.0662, and 82.54%, respectively. The scattering angle, number of averaged pixels, length of timesteps, and radiative and polarized fitting residuals showed impacts on the results of AOD retrieval in the DPC GRASP/Models. From the most AERONET sites, the R and EE% were larger than ~0.9 and ~80%. Compared with MODIS products, the spatial and temporal variations of aerosol could be caught by the DPC with the GRASP/Models, showing a good performance. However, values of AOD were also underestimated by DPC, probably due to overstrict cloud mask. The above findings validated the ability of the DPC sensor to monitor aerosols. It should contribute to the development of aerosol parameter retrieval from multi-angular polarized sensors in the future.

Key Words: GRASP/Models, Aerosol Optical Depth, Directional Polarimetric Camera, GaoFen-5,

42 **1. Introduction**

43 Aerosol is one of the most important components in the atmosphere. They influence the global
44 radiation budget balance and climate directly by scattering and absorbing incoming solar radiation
45 and indirectly by changing cloud microphysical properties (Albrecht 1989; Rosenfeld et al. 2008).
46 Due to the different emission sources and relatively transitory lifecycle in the atmosphere, aerosol
47 particles show large spatiotemporal variability, and are difficult to describe uniformly at a global
48 scale (Eck et al. 2010; Jin et al. 2019; Ma et al. 2021). This property can further affect atmospheric
49 motions, the hydrological cycle, and probably contribute to regional extreme weather events (Guo
50 et al. 2016; Li et al. 2016; Nakajima et al. 2007; Shi et al. 2021). Therefore, the development of
51 aerosol measurement technologies has received widespread attention in recent decades.

52 Satellite observation is the main approach to monitor and quantify aerosol distributions at a
53 global scale (Kaufman et al. 1997). Traditional satellite technology relies on prior assumptions about
54 the properties of the surface and atmosphere, because the prerequisite for successful retrieval of
55 aerosol is that the aerosol signal should be isolated from the remainder of the signal received by
56 satellite, which includes the combined effect from molecule, aerosol, cloud, and the underlying
57 surface (Lenoble et al. 2013). For instance, the appropriate spatial resolution helps to observe
58 aerosol through clear holes in otherwise cloudy skies (Jin et al. 2021). The choice of spectral channel
59 and bandwidth can avoid impact by gas absorption in narrow spectral bands known as atmosphere
60 window regions. More importantly, the spectral channel should be set in a carefully selected band
61 to avoid introducing uncertainty from underlying surface features, such as vegetation, bright desert,
62 and ocean color (Hsu et al. 2004; McCormick et al. 1979; Rao et al. 1989). Based on these principles,
63 a series of aerosol products from different sensors have been released, and they greatly promote the
64 developments of studies in aerosol-related fields, including aerosol climate effect, interaction of
65 aerosol and cloud, air quality and public health, and global climate modeling (Gao et al. 2017; Liu
66 et al. 2022; Sayer et al. 2013; Tegen and Lacis 1996; Zhang et al. 2021).

67 With the progress of satellite technology, sensors with broader spectral range, multiple angles,
68 and polarization observations have been applied to aerosol observations (Dubovik et al. 2019).
69 POLDER-3 is the third sensor in the POLarization and Directionality of the Earth's Reflectance
70 series, carried on the Polarization and Anisotropy of Reflectances for Atmospheric Science coupled
71 with Observations from a Lidar (PARASOL), which was launched on December 18, 2004, as part
72 of the A-Train (Tanre et al. 2011). This instrument views ($\pm 51^\circ$ along track and $\pm 43^\circ$ across track)
73 Earth from ~ 14 different angles by using a set of wide-field telecentric optics and a rotating filter
74 wheel in nine spectral channels from 443 to 1020 nm (Deschamps et al. 1994). Among them, three
75 channels at 490, 670, and 865 nm have polarization observation capabilities. POLDER-3 provides
76 the longest multi-angle polarimetric observation record of the Earth-atmosphere system in space to
77 date and the PARASOL mission was terminated in December 2013 due to limited on-board fuel.
78 The Directional Polarimetric Camera (DPC) is the first Chinese multi-angle polarized Earth
79 observation satellite sensor, onboard the fifth satellite (GaoFen-5) of the Chinese High-resolution
80 Earth Observation Program (Li et al. 2018). It was launched successfully on May 9, 2018, with the
81 purposes of measuring aerosol parameters and providing information for the assessment of urban
82 air pollution. The design of DPC is similar to the POLDER-3. It is equipped with five non-polarized

83 bands at 443, 565, 763,765, and 910 nm and three polarized bands at 490, 670, and 865 nm, with a
84 relatively high spatial resolution of 3.3 km, that can observe Earth from ~9 different angles.
85 Therefore, the DPC occupies an important position in the development of polarization instruments
86 in China, and is expected to provide beneficial information for atmospheric aerosol monitoring and
87 satellite payload research.

88 The multi-angular polarized sensor can provide many more observations for the same pixel in
89 an aerosol parameter retrieval. Compared to traditional spectral measurement, the multi-angle can
90 help constrain bidirectional reflections function, reducing uncertainty from the surface (Diner et al.
91 1998), while the polarized signal is mainly from atmospheric aerosol and sensitive to particle
92 microphysical properties (Mishchenko and Travis 1997). Generally, the polarized signal can be
93 considered as an independent source of information. A well-known advantage is that the polarized
94 light from the surface accounts for a small part of the total polarized light compared with that from
95 the particles and is mostly wavelength independent. In the algorithms for POLDER, the polarized
96 signals at 670 and 865 nm are used for deriving the best aerosol model over the ocean and retrieving
97 Aerosol Optical Depth (AOD) over land, due to the sensitivity to fine particles (Deuzé et al. 2001;
98 Ge et al. 2020; Kacenelenbogen et al. 2006; Nadal and Bréon 1999). In addition, the existence of
99 the cloudbow effect in the polarized signal can also be used to recognize cloud mask and detect
100 cloud structure (Breon and Colzy 1999; Breon and Goloub 1998; Li et al. 2021).

101 However, the algorithms that retrieve aerosol parameters from only one or two polarized
102 channels struggle to obtain complex aerosol optical and microphysical parameters, such as aerosol
103 size distribution and absorbing and scattering properties. To solve this problem, the Generalized
104 Retrieval of Atmosphere and Surface Properties (GRASP) algorithm was developed, which provides
105 a statistical optimized strategy that allows all aerosol-related measurement data from multi-angular
106 polarized sensors to participate in the retrieval (Dubovik et al. 2014). It points out that the measured
107 redundancy provided by multi-angular polarized sensor is considered to be positive and useful,
108 especially when the number of observations is larger than the unknowns (Dubovik et al. 2011). At
109 present, the GRASP algorithm has been successfully applied to a variety of sensors, including
110 POLDER, lidar, and sun photometer, to retrieve complex aerosol parameters (Chen et al. 2020; Li
111 et al. 2019; Lopatin et al. 2021). In this study, we retrieved AOD from DPC observations by using
112 GRASP algorithm and evaluated possible error influencing factors. At the same time, by comparing
113 MODIS and AERONET observations, the aerosol monitoring performance of DPC were verified in
114 different space and time scales. This will partially lay the foundation for the retrieval of aerosol
115 parameters from multi-angular polarized sensors in the future of China.

116 **2. Satellite and Ground-based Data**

117 **2.1 DPC Data**

118 The DPC is a multi-angular polarized sensor carried on the GF-5 satellite, which was launched
119 in May 9, 2018. This sensor completes a scan of entire Earth's surface about every two days from a
120 sun-synchronous orbit and provides a swath of 1850 km with a spatial resolution of 3.3 km (Li et
121 al. 2018). The DPC contains eight bands from 443 to 910 nm with a bandwidth of 10-40 nm that
122 can observe Earth from ~9 different angles in a local time of ~13:30 PM. Along with channels for
123 water vapor (910 nm) and pressure (Oxygen A band: 763 and 765 nm), five bands (443, 490, 565,

124 670, and 865 nm) are designed to measure aerosols (Li et al. 2018). The polarimetric capability at
125 490, 670, and 865 nm is realized by a polarized filter wheel (0° , 60° , and 120°) and a step motor
126 (Hagolle et al. 1999). The laboratory calibration uncertainties are 5% for normalized radiation and
127 0.02 for Degree Of Linear Polarization (DOLP) (Li et al. 2021). An in-flight calibration study
128 showed that the radiometric calibration error increased to $\sim 9\%$ at 865 nm and the polarimetric
129 calibration error increases to ~ 0.04 at 490 and 670 nm after launch, by respectively applying
130 Rayleigh and glint scenes over ocean (Qie et al. 2021). Degradation of instrument performance over
131 time may result in higher negative radiometric shift (Zhu et al. 2022). Thus, additional correction
132 coefficients were also applied in this study to correct the image of the DPC observations from March
133 to April, 2020. The processing of DPC data is described in Section 3.2 in detail.

134 2.2 MODIS aerosol products

135 The Moderate-resolution Imaging Spectroradiometer (MODIS) has been in service for over
136 two decades, providing valuable Earth observations. The MODIS Level 2 C6.1 aerosol product
137 (MxD04) is generated by using Dark Target (DT) algorithm and Deep Blue (DB) algorithm (Hsu et
138 al. 2013; Levy et al. 2013). It provides multi-wavelength AOD data from each individual image
139 with spatial resolutions of 3 km and 10 km. The MODIS Level 2 C6 aerosol product (MCD19A2)
140 calculates aerosol parameters by using the Multi-Angle Implementation of Atmospheric Correction
141 (MAIAC) algorithm from the continuous scenes of two satellites (Terra and Aqua) and considers
142 temporal and spatial correlation of aerosols, with spatial resolution of 1 km (Lyapustin et al. 2018).
143 DT algorithm provides retrievals over ocean and land except for bright surfaces (such as desert dust),
144 while the DB algorithm is only applied over land, and the MAIAC algorithm is used over land and
145 part of the surrounding ocean. These MODIS aerosol products have been rigorously tested and
146 verified, and are widely used in aerosol-related studies (Che et al. 2019; Sayer et al. 2014; Zhdanova
147 et al. 2020). In this study, the corrected AOD (quality flag = 3) on land and average AOD (quality
148 flag = 1,2,3) on the ocean are selected from the DT products. The best estimated AOD (quality flag
149 = 2,3) is selected in the DB products. The best quality AOD (QA AOD = 0000) is selected in the
150 MAIAC products.

151 2.3 AERONET observations

152 The AERosol RObotic NETwork (AERONET) is a federation of ground-based remote sensing
153 aerosol networks, established and expanded by various institutions from different countries (Holben
154 et al. 1998). It has contributed continuous and long-term aerosol optical, microphysical, and
155 radiative properties for more than 25 years in major ecosystems and human activity areas around
156 the world. The AOD data used for validation were acquired from 178 AERONET sites with Level
157 2.0 AOD products, which have been cloud-screened and quality controlled. The uncertainties of
158 AOD are less than 0.02 (Eck et al. 1999). In order to match the AERONET data to the satellite
159 observations, a common approach is followed to average satellite data within ± 30 min and a circle
160 of 0.25° (~ 25 km) radius centered at the selected site (Sayer et al. 2013). The relationship between
161 multi-wavelength AOD proposed by Ångström (1964) was applied to calculate the AOD at
162 corresponding wavelength of satellite bands from AERONET data.

163 3. Methods

164 3.1 Introduction of GRASP algorithm

165 GRASP is an open-source software package (<https://www.grasp-open.com/>) for calculating
166 and retrieving various optical and microphysical properties of aerosol and surface from observations
167 of different remote sensing instruments, such as satellite, lidar, radiometer, and radiosonde (Dubovik
168 et al. 2021). It was originally designed to solve the problem of aerosol retrieval from the PARASOL
169 observations (Dubovik et al. 2014), while now has become a scientifically rigorous and versatile
170 algorithm based on generalization principles that works with diverse remote sensing applications in
171 the community after continuous development (Dubovik et al. 2021). The GRASP algorithm contains
172 two pivotal and independent modules. One is used to calculate the scattering, absorption, and
173 extinction of light between different media from the physical level, simulating theoretical
174 observational radiation signal, called “Forward Model”. It allows definition of various complex
175 aerosol (size distribution, refractive index, and sphere fraction, etc.) and surface properties
176 (Bidirectional Reflectance/Polarization Distribution Function, BR/PDF, etc.) in the construction of
177 the modelled reflectance. Therefore, it is possible to transform from optical observations to aerosol
178 microphysical properties and estimate the surface parameters (Dubovik et al. 2011). The other
179 module can be thought of as general mathematical operations without any particularly physical
180 nature, called “Numerical Inversion”. It follows the statistically optimized strategy to fit
181 observations under the fundamental frameworks of the Maximum Likelihood Method and multi-
182 term Least Square Method (Dubovik and King 2000). GRASP also realizes multiple-pixel retrieval,
183 which constrains the variability of aerosol and surface optical properties in fitting process by an
184 extra prior knowledge. Due to the consideration of the surrounding pixel information, the multi-
185 pixel retrieval is more stable, and more importantly, it can make up for the lack of aerosol reflection
186 information in some cases, such as conditions that the signal from aerosol is much less than that
187 from the surface (Dubovik et al. 2011). Based on the above advantages, the GRASP supports input
188 measurements/parameters from different sources and levels, such as normalized and polarized
189 radiance, vertical extinction and backscatter profile, and optical depth. This avoids that the most
190 popular look-up table-based methods are difficult to apply to each other, due to the limitations of
191 different sensor channel and characteristic.

192 3.2 Pre-processing of DPC Data

193 In order to partially offset the signal attenuation due to instrument aging, before the pre-
194 processing and retrieval, the radiance signals from the DPC were transferred and corrected to
195 normalized radiative and polarized reflectance at top of the atmosphere, as equation 1.

$$196 [I_N, Q_N, U_N]^T = \pi \cdot [I, Q, U]^T / [E_0 \cdot A'_k(\theta_0) \cdot P'_k(\theta)] \quad (1)$$

197 where, the $[I, Q, U]^T$ represent the radiative and polarized radiances, received by the DPC, in the
198 form of the first three parts of the Stokes vector. The $A'_k(\theta_0)$ and $P'_k(\theta)$ are the two additional
199 correction coefficients. For I , they are applied following the results of Zhu et al. (2022), which
200 depends on the view zenith angle (θ) and calculated based on Rayleigh scenes over sea surface. For
201 polarimetric signals, the additional correction coefficients can be referred to Qie et al. (2021). The
202 E_0 is the standard solar radiation flux and the $[I_N, Q_N, U_N]^T$ are the corrected normalized signals
203 at top of the atmosphere of DPC.

204 In successful AOD retrieval, one of the key processes is to screen appropriate pixels. Cloudy
 205 pixels are the main factor impacting aerosol retrieval, because they will block the signal from aerosol
 206 due to high reflectance, large coverage, and relatively high vertical position. Even very thin cirrus
 207 clouds and missed cloud edges can cause an positive error of ~13% in visible channel (Koren et al.
 208 2007). To remove cloud pixels in DPC images, we used several universal methods by considering
 209 cloud-sensitive characteristics in radiative and polarized bands:

210 1) The first step is to filter the image with a 3×3 sliding window at the blue (490 nm) and red
 211 (670 nm) bands for land and sea surfaces, respectively (Remer et al. 2012). If the standard deviation
 212 of a window is greater than 0.0025, then the center pixel will be marked as a cloud pixel and removed
 213 (Martins et al. 2002). This method was initially applied to the MODIS image by considering the
 214 spatial variability of aerosol and cloud pixels. In addition, a threshold of > 0.4 in the green (565 nm)
 215 band is also used to detect cloud pixels after the filter process, in accordance with the DT algorithm.
 216 This threshold is to exclude very uniformly distributed cloud pixels in the central area of thick clouds,
 217 and some snow pixels and glint area will also be excluded at the same time.

218 2) In second step, a whiteness test was applied by using reflectance in visible bands. It uses the
 219 characteristic that clouds are white in the visible band, considering that pixel with the absolute value
 220 of relative deviations greater than 0.7 is cloud, as equation 2-3.

$$221 \quad \text{MeanVis} = (\text{Band}_1 + \text{Band}_2 + \text{Band}_3)/3 \quad (2)$$

$$222 \quad \text{Whiteness Test} = \sum_{i=1}^3 |(\text{Band}_i - \text{MeanVis})/\text{MeanVis}| > 0.7 \quad (3)$$

223 Where, Band_1 , Band_2 , and Band_3 are reflectance in red, green, and blue bands received by
 224 satellite at top of the atmosphere, respectively. Corresponding to the DPC, they are 490, 565, and
 225 670 nm, respectively. In the absence of infrared and thermal infrared information, it can
 226 supplementally remove any pixels that have flat reflectance, similar to some operators using
 227 reflectance ratio to detect clouds. This method was proposed by Gomez-Chova et al. (2007) for
 228 Medium Resolution Imaging Spectrometer (MERIS) multispectral image, and it has also been
 229 considered in the well-known Fmask algorithm (Zhu and Woodcock 2012).

230 3) The third step used polarized bands to remove cloud pixels, following a fact that cloud drops
 231 can show a relatively strong polarized reflectance by multiple scattering (cloudbow effect) under a
 232 specify observation geometry. This feature has been used to a generate cloud mask product for both
 233 POLDER and DPC sensors (Breon and Colzy 1999; Li et al. 2021). When the scattering angle (SCA)
 234 is between 127° and 157°, pixels with corrected polarized radiation at 865 nm larger than 0.03 and
 235 0.05 for ocean and surface, respectively, are defined as cloud (Li et al. 2021). The relatively large
 236 SCA range is for a strict screening, given that the main peak of the polarized reflectance by cloud
 237 water droplets is ~142° (Goloub and Deuze 1994). In addition, any obvious noise is also removed
 238 in this step, such as the case of DOLP > 1.

239 3.3 Construction of Multi-pixel Retrieval Unit

240 Next, we will explain the necessary operations and settings of parameters to apply the GRASP
 241 algorithm to DPC data in detail. The GRASP algorithm can use the temporal and spatial continuity
 242 of pixels, and allow a group of pixels to be inverted at the same time. The multi-pixel retrieval unit
 243 for DPC in the study is shown as **Figure 1**. Each small cube represents a pixel in geographic grids
 244 with a spatial resolution of 0.1°×0.1° (3×3 DPC pixel averaged). This is in accordance with the
 245 MODIS 04_L2 product (~10 km). The projection is determined by the DPC data. Each pixel is
 246 guaranteed to have at least 3 different observation angles. Size of the retrieval unit can be arbitrarily

247 selected, but is limited by the hardware memory. Different colors show the percentage of land or
248 sea, and usually do not change with time. They need to be clearly defined in GRASP to select
249 different surface reflectance models. Cloud and no-data pixels need to be removed before the
250 retrieval, because the cloud flag setting has not been implemented in the current version of code.
251 Finally, this retrieval unit was processed using the GRASP algorithm to derive the AOD
252 distributions.

253 3.4 Settings of Retrieval Parameters

254 The settings of initial value and spatial-temporal constraint can significantly impact results of
255 the statistically optimized strategy in the GRASP algorithm (Dubovik et al. 2011). The GRASP
256 allows several strategies to fit observations. For instance, the GRASP software gives two retrieval
257 schemes for POLDER observations. The configurations of the two schemes are different only by
258 settings of aerosol size distribution in the forward model. One fits the aerosol size distribution with
259 16 triangle bins from the range of 0.05 to 15.0 μm , while the other uses 5 lognormal bins at 0.1,
260 0.1732, 0.3, 1.0, and 2.9 μm , based on pre-calculated optimized kernels of the POLDER-3. The 5
261 lognormal bins scheme increases speed by ~ 9 times (2.5GHz CPU) without any
262 graphical acceleration compared to the 16 triangle bins scheme, and it has been used to generate the
263 operational PARASOL/GRASP aerosol products (Chen et al. 2020). In addition, there is a scheme
264 that is being tested called “GRASP/Models”. The GRASP/Models approach assumes an external
265 mixture of several aerosol types with fixed optical parameters, which is fast and more stable AOD
266 retrieval especially when aerosol loading is low (Chen et al., 2020).

267 A tolerable absolute error in radiative transfer calculations is set to 0.0005 and the multiple
268 scattering effects have been considered. The number of atmospheric layers is set to 10 with an
269 exponential distribution. The input data of the GRASP algorithm was both normalized radiative
270 measurements at 443, 490, 565, and 670 nm and DOLP of 490 and 670 nm. The initial guess of
271 aerosol and surface properties are default in the GRASP software. They are applied to calculate
272 AOD at a global scale. The Ross-Li’s model (Li and Strahler 1992) and the Cox-Munk model (Cox
273 and Munk 1954) were used for modeling radiative (non-polarized) reflectance over land and ocean,
274 respectively, while, the surface polarized reflectance followed the method of Nadal and Bréon
275 (1999). More details are documented in Dubovik et al. (2011). Among them, the complex refractive
276 index and surface properties are generally allowed to be fit as wavelength-dependent parameters in
277 iterations. All constraints on values are given a default sizeable range, such as the first parameter in
278 the Ross-Li’s model allowed to vary from 0.001 to 1.100. By light scattering calculations (Dubovik
279 et al. 2006), all aerosol microphysical parameters are converted into optical parameters to participate
280 in radiative simulation. Spatial and temporal constraints of variabilities of aerosol and surface
281 properties are realized using Lagrange multiplier method. More details can be referred to Dubovik
282 et al. (2021). In this study, the GRASP/Models scheme was used to retrieve AOD from DPC. All
283 calculations of the GRASP relied on the supercomputing system in the Supercomputing Center of
284 Wuhan University.

285 4. Results and Discussions

286 4.1 Validation of DPC/GRASP with AERONET

287 As shown in **Figure 2**, the AERONET observations were used as the references to estimate the
288 performance of AOD retrieval from DPC images based on the GRASP algorithm. Linear regression,
289 correlation coefficient (R), Root Mean Square Error (RMSE), Mean Bias (MB), percentage falling
290 into Expected Error (EE%, $\pm(0.05+0.15*AOD)$), and matching Number (N) were also calculated.
291 Among them, the EE% is selected in accordance with the MODIS error envelop and the ideal EE%
292 is ~68% under assumption of normal distribution within one sigma confidence interval. Overall, the
293 DPC GRASP/Models AOD matches the AERONET observations with an R of 0.8511, a MB of
294 0.0256, and a RMSE of 0.0842, showing good performance without any quality control. Nearly 80%
295 of the GRASP/Models AOD retrievals fall within the EE% bounds, revealing that the error envelop
296 of DPC is probably narrower than that of MODIS. While, the slope of linear regression was 0.8686,
297 less than 1. This means that under heavy aerosol loading, the DPC/GRASP probably underestimates
298 the AOD. More details are presented in **Figure 2c**. It is found the lower slope of linear regression is
299 mainly controlled by several points which have larger AOD (> 0.8). By contrast, when AOD is less
300 than 0.8, the retrieval is stable.

301 In order to further study the retrieval performance of GRASP/Models and control the quality
302 of the retrieval result from DPC data, we calculated the dependences of absolute MB with retrieval
303 residuals, timesteps (serial length) and average pixel (involved in retrieval) number in retrieval units,
304 and observation geometry, as shown in **Figure 3**. The retrieval absolute MB showed an obvious
305 increase when the SCA is larger than 150° . Critical observation conditions, such as pixels at the
306 edge of the image, will probably result to a larger error in both satellite sensor and forward model.
307 By contrast, different viewing angle number (3-11) have relatively little impact on the retrieval
308 results, with the absolute MB per bin ranging between 0.0296 and 0.0595. With increase in timesteps,
309 the absolute MB showed a slightly decreasing trend, from 0.0543 to 0.0561. The same phenomenon
310 was also found in the **Figure 3d**. The absolute MB decreased from 0.0691 to 0.0435 with the number
311 of averaged pixels increasing. This indicated that the fitting scheme for using the external mixing
312 of different aerosol types in this scheme of the GRASP/Models showed positive dependence of the
313 length of timesteps and number of pixels. In addition, the spatial-temporal constraints in the retrieval
314 are also affected by Lagrange multipliers, which can be customized in the configuration file.

315 Fitting residual is an important factor to estimate the quality of retrieval in GRASP. It was
316 found that the absolute MB showed a slight increase (from 0.0397 to 0.0596) when the radiative
317 fitting residuals were larger than 8%. The absolute MB had a trend to decrease first and then increase,
318 with increase in the polarized fitting residuals. Given that the DPC designed uncertainty is about 5%
319 for radiometric measurements and 0.02 for DOLP, the relatively large absolute MB (0.069) at 0.01
320 of the polarized fitting residuals is probably caused by the noise. To summarize, the SCA, number
321 of averaged pixels, and fitting residuals showed the impacts on DPC GRASP/Models AOD retrieval
322 in this test. Retrieval is considered low quality if any of the following conditions are met: 1) Pixels
323 with SCA > 150 ; 2) number of averaged pixels < 4 ; 3) length of timesteps < 5 ; 4) non-polarized
324 fitting residual $> 8\%$; 5) polarized fitting residual > 0.06 .

325 **Figure 4a-b** shows the scatterplots and density distributions of DPC/GRASP AOD versus the
326 AERONET observations after quality control. About 20% of the points were removed. It was found
327 that the performance of AOD retrieval from DPC images showed an enhancement. For DPC
328 GRASP/Models, the R increased from 0.8511 to 0.9001, the EE% increased from 79.30% to 82.54%,
329 the RMSE decreased from 0.0842 to 0.0662, and the MB decreased from 0.0256 to 0.0234. **Figure**
330 **4c** displays the changes of differences between DPC and AEROENT AOD. The underestimations

331 when AOD > 0.8 were not found to be restrained by the quality control. A possible reason is that an
332 overly restrictive cloud mask can remove aerosol pixels during heavy pollution. In addition, the
333 negative drift after the launch of the DPC may also be the reason, if it is not fully corrected.

334 4.2 Evaluation of DPC AOD Performance at a Spatial Scale

335 The DPC AOD retrieved by the GRASP/Models were compared with AERONET observations
336 at each individual site to show a world-wide retrieval result as **Figure 5**. The R, RMSE, MB, and
337 EE% were calculated and displayed for sites where the matching number of pixels was larger than
338 5. In addition to the observation performance of the DPC itself, spatial variations in performances
339 of AOD retrieval greatly depend on settings of initial parameter and constraint in the GRASP,
340 whether they are in line with the local aerosol and surface environments. Results showed that the
341 GRASP/Models achieved a great performance in different regions. The high values of R (> 0.8)
342 were found in most regions, while the lower values (~0.6) were mainly observed in North America.
343 The values of RMSE at most sites were less than 0.08. These suggest that most values of AOD
344 retrieval matched the AERONET AOD very well. At several sites, such as Asia and Africa, the
345 RMSE were larger than 0.2, revealing that the AOD has a relatively larger deviation calculated from
346 DPC images based on current parameter setting with the GRASP algorithm in the regions. From the
347 MB of **Figure 5c**, the values of AOD were overestimated (~0.04) in most areas. By contrast, the
348 underestimations were found in high aerosol loading regions, such as South Asia and North Africa,
349 that MB values were between -0.02 and -0.10, in accordance with the large underestimation when
350 AOD > 0.8 mentioned above. The EE% showed that over 80% of AOD retrieved in sites can fall
351 within the expected error range. It is worth noting that the parameterization in the GRASP/Models
352 scheme is a globally consistent configuration in this study and does not consider the characteristics
353 between different regions. This means that it is possible to achieve better results in local regions by
354 adjusting different parameterizations.

355 To further estimate the performance of DPC/GRASP AOD, two regions were selected as cases
356 as shown in **Figure 6**. The MODIS MAIAC, DT, and DB aerosol products were used as comparisons.
357 It was noted that the DB algorithm was only executed over land in the C6.1 MODIS DB aerosol
358 products. It was found that the spatial coverage of GRASP/Models AOD from DPC over land was
359 slightly lower than the MAIAC MODIS aerosol products. In addition to the narrower field of view
360 and longer re-visit cycle on DPC (MODIS operated in two satellite: Terra and Aqua), the cloud mask
361 method probably also mis-classified the cloud-free pixels in heavy aerosol loading conditions. This
362 also partially resulted in the underestimation of DPC AOD because the heavy aerosol loading pixels
363 are removed. Nevertheless, DPC still properly captures the spatial distribution of AOD. The highest
364 AOD values (> 1.0) in the southern part of China (mainly Guangdong and Guangxi) were caught
365 by the current retrieval strategy. This is in accordance with the three MODIS products. By contrast,
366 the AOD found in North China Plain and Centre China by the DPC GRASP/Models (~0.5) were a
367 little bit lower than MAIAC and DT products (~0.6). However, the DT aerosol products showed
368 higher AOD in this region, closed to ~1.0. This phenomenon is caused by unsuitable aerosol models,
369 which further results in a persistent overestimation in the DT algorithm (Che et al. 2019). By the
370 additional radiometric and polarimetric correction, the DPC GRASP/Models showed good
371 performance over both Land and Ocean. The high values of AOD in the South China Sea and the
372 estuary of the Yangtze River can be clearly captured. To summarized, the DPC showed spatial ability
373 of AOD retrieval based on GRASP algorithm in China region and the similar results have also been

374 reported recently by using the GRASP/component module (Li et al. 2022).

375 Another case was selected in Western Europe where the air is clean and aerosol loading is low
376 (< 0.2) most of the year. As shown in **Figure 6b**, different satellites and aerosol retrieval methods
377 showed slightly different distributions of AOD. In addition to the different transit times between
378 DPC and MODIS, this phenomenon is also probably because the aerosol signal is difficult to
379 separate from the remainder of signal under low aerosol loading conditions and thus result in relative
380 larger uncertainties of retrieval. From the AOD maps of DPC GRASP/Models, the relatively high
381 values of AOD (~ 0.25) were found in Central France, Southern Spain, and Southern England. While,
382 the MODIS MAIAC showed lower AOD (~ 0.1) over the mainland and two points of high AOD
383 (~ 0.5) were found in Northern coastal areas of Spain and Algeria. By contrast, the distributions of
384 AOD calculated by DT and DB algorithm were also different from that calculated by DPC
385 GRASP/Models and MAIAC. The high AOD (~ 0.4) region appeared in Northern France, Italy, and
386 Southern England. Compared with single pixel-based retrieval algorithm (such as DT and DB), the
387 GRASP and MAIAC considered more temporal and spatial information of aerosol and surface
388 parameters. And benefit from the consistency of all assumptions (regarding aerosol and a priori
389 constrains), the DPC GRASP exhibits minimal land-sea contrast. All of them have been proven to
390 have good performance of AOD retrieval (Chen et al. 2020; Lyapustin et al. 2018; Ou et al. 2021;
391 Sayer et al. 2014).

392 **Figure 7** shows density distributions of difference between DPC and MODIS products in
393 ranges of $AOD \leq 0.2$, $0.2 < AOD \leq 0.7$, and $AOD > 0.7$. Corresponding to the **Figure 6**, this is
394 used to complement quantitative evaluations for the two regions. A common pattern is seen in all
395 sub-plots, namely that the differences were nearly normally distributed, centered on the 0 under low
396 aerosol loading conditions ($AOD \leq 0.2$). With increasing AOD ($AOD > 0.7$), the differences
397 showed an increasing negative bias, with the peak value varying from -0.5 to -1.0. The DPC
398 GRASP/Models underestimated AOD under heavy aerosol loading conditions, similar to the
399 comparisons with AERONET. In follow-up studies, a more detailed investigation of this problem is
400 required.

401 4.3 Comparison of DPC AOD with MODIS Products at a Temporal Scale

402 In this section, time-series of AOD were evaluated against MODIS aerosol products based on
403 the observations of AERONET site. The time-series of daily RMSE is calculated for the global
404 AERONET data set, as shown in **Figure 8**. Lower value of RMSE means the smaller actual errors,
405 indicating a good match with the AERONET. The AERONET stations had relatively continuous
406 observations during the study period to avoid how global validation statistics shift with the spatial
407 distribution of observations (Gupta et al. 2018). From the **Figure 8**, it was found that the time series
408 of AOD from DPC GRASP/Models had a good matching with the AERONET AOD. The values of
409 RMSE were ~ 0.06 and stable before 87th day. While the reason of relatively large RMSE (~ 0.12)
410 around 90th day is presumed to be heavy aerosol loading conditions, as the DPC GRASP/Models
411 would underestimate AOD under this situation. The similar temporary rapid increases in RMSE
412 were also found in MODIS products, such as the 80th day of the DT, the 85th day of the DB, and 98th
413 day of the MAIAC. This reflects the time instability of algorithms. In addition, the lowest daily
414 averaged RMSE was found in DPC GRASP/Models with value of 0.0663, and then MODIS DT
415 (0.0863) and MODIS DB (0.0913). The low RMSE of DPC may be due to it ignoring some high
416 value AODs. It is worth noting that the same parameter scheme (including start points and

417 constraints) was applied globally in the GRASP/Models. Therefore, the difference in aerosol optical
418 properties and spatial-temporal heterogeneity in different regions may be not considered
419 appropriately. The optimization of the region is expected to improve the retrieval effect and further
420 evaluation also requires the use of longer sequences of DPC data in the future.

421 **Figure 9** shows three cases at different underlying surface to display the time series of AOD
422 retrieved from DPC GRASP/Models on the basis of AERONET observations. The DT AOD was
423 also compared as a reference, due to its stable performance. It was found that the behavior of AOD
424 from DPC/GRASP and MODIS DT was generally consistent with AERONET at the three sites.
425 From the scatterplots, the values of R were 0.947 and 0.949, 0.943 and 0.959, and 0.967 and 0.859
426 for MODIS DT and DPC GRASP/Models AOD at Raciborz, Magurele_Inoe, and FZJ-JOYCE,
427 respectively. The GRASP/Models AOD retrieved from DPC were slightly higher than the
428 AERONET in the FZJ-JOYCE site and thus it resulted a relatively lower R. Nevertheless, in general,
429 DPC/GRASP has a good ability to capture the temporal variation of aerosols.

430 **Conclusion and Summary**

431 The DPC/GaoFen-5 is the first multi-angular polarized sensor launched by China and thus it
432 has occupied an important position in the development of satellite sensors. In this study, AOD was
433 retrieved from the DPC images by using the GRASP algorithm and compared with AERONET and
434 MODIS observations. The main purpose was to evaluate the performance of the DPC to monitor
435 global aerosols.

436 On a global basis, a uniform parameterization scheme, which defined the variation ranges and
437 start values of the optical and microphysical properties (realized by aerosol type) of the aerosol, was
438 applied in the “Model” module of GRASP. Validations against AERONET showed that the R and
439 EE% of DPC GRASP/Models were 0.8511 and 79.30%, respectively, in the first attempt. The SCA,
440 number of averaged pixels in retrieval units, and fitting residual showed an impact on the results of
441 AOD. A larger number of pixels in retrieval units and a smaller fitting residual can help improve the
442 quality of retrieval. By quality control (removing pixels: $SCA > 150$; number of averaged pixels $<$
443 4 ; length of timesteps < 5 ; non-polarized fitting residual $> 8\%$; polarized fitting residual > 0.06), the
444 R and EE% of DPC GRASP/Models AOD improve to 0.9007 and 82.54%, respectively. The
445 corresponding MB and RMSE decreased from 0.0256 and 0.0842 to 0.0234 and 0.0662, respectively.
446 This indicated that DPC has a good ability to detect aerosols under this scheme.

447 In the perspective of spatial scale, the R and EE% of GRASP/Models were larger than 0.9 and
448 80% respectively at most AERONET sites. Large RMSE and Low EE% were found in heavy aerosol
449 loading conditions such as Asia and Africa. When the actual AOD was large, the retrieval bias of
450 AOD from satellite observations would be amplified as reflected in RMSE and EE% to some extent.
451 By compared with MODIS aerosol products, the AOD from DPC GRASP/Models showed good
452 consistency in China, with all heavy aerosol loading regions were detected. However, the values of
453 AOD were underestimated by DPC, probably due to overstrict cloud masking. Evaluation of the
454 time-serial AOD showed the performance of DPC GRASP/Models was similar to the MODIS DT
455 and better than MODIS DB and MAIAC products. Therefore, to summarize, the DPC could capture
456 spatial and temporal variations in aerosols. The study improves to our understanding of DPC and
457 finds a solution for retrieving AOD based on GRASP algorithm. The continuous development of
458 multi-angle sensors polarized plays an important role in aerosol monitoring in the future.

459 **Acknowledgement**

460 This study was funded by the National Key R&D Program of China (Grant No. 2018YFB0504500),
461 National Natural Science Foundation of China (Grant No. 41875038, No. 42071348, and No.
462 42001291), the Key R&D projects in Hubei Province (Grant No. 2021BCA220) and supported by
463 the LIESMARS Special Research Funding. We are grateful to the Moderate Resolution Imaging
464 Spectroradiometer (MODIS) Team, the Aerosol Robotic Network (AERONET) Organization and
465 the GaoFen-5 Directional Polarimetric Camera (DPC) Developed Team for freely distributing their
466 aerosol products and measurements. The numerical calculations in this paper have been done on the
467 supercomputing system in the Supercomputing Center of Wuhan University. Finally, we would also
468 like to thank all reviewers for their constructive and valuable comments.

469 **References**

- 470 Albrecht, B.A. (1989). AEROSOLS, CLOUD MICROPHYSICS, AND FRACTIONAL CLOUDINESS.
471 *Science*, 245, 1227-1230, doi:10.1126/science.245.4923.1227
- 472 Ångström, A. (1964). The Parameter of Atmospheric Turbidity. *Tellus*, 16, 64-75,
473 doi:10.3402/tellusa.v16i1.8885
- 474 Breon, F.M., & Colzy, S. (1999). Cloud detection from the spaceborne POLDER instrument and
475 validation against surface synoptic observations. *Journal of Applied Meteorology*, 38, 777-785,
476 doi:10.1175/1520-0450(1999)038<0777:cdfstp>2.0.co;2
- 477 Breon, F.M., & Goloub, P. (1998). Cloud droplet effective radius from spaceborne polarization
478 measurements. *Geophysical Research Letters*, 25, 1879-1882, doi:10.1029/98gl01221
- 479 Che, H., Yang, L., Liu, C., Xia, X., Wang, Y., Wang, H., Wang, H., Lu, X., & Zhang, X. (2019). Long-
480 term validation of MODIS C6 and C6.1 Dark Target aerosol products over China using CARSNET and
481 AERONET. *Chemosphere*, 236, 124268, doi:10.1016/j.chemosphere.2019.06.238
- 482 Chen, C., Dubovik, O., Fuertes, D., Litvinov, P., Lapyonok, T., Lopatin, A., Ducos, F., Derimian, Y.,
483 Herman, M., Tanré, D., Remer, L.A., Lyapustin, A., Sayer, A.M., Levy, R.C., Hsu, N.C., Descloitres, J.,
484 Li, L., Torres, B., Karol, Y., Herrera, M., Herreras, M., Aspetsberger, M., Wanzelboeck, M., Bindreiter,
485 L., Marth, D., Hangler, A., & Federspiel, C. (2020). Validation of GRASP algorithm product from
486 POLDER/PARASOL data and assessment of multi-angular polarimetry potential for aerosol monitoring.
487 *Earth System Science Data*, 12, 3573-3620, doi:10.5194/essd-12-3573-2020
- 488 Cox, C., & Munk, W. (1954). Measurement Of The Roughness Of The Sea Surface From Photographs
489 Of The Sun's Glitter. *Journal Of The Optical Society Of America*, 44, 838-850,
490 doi:10.1364/JOSA.44.000838
- 491 Deschamps, P., Breon, F., Leroy, M., Podaire, A., Bricaud, A., Buriez, J., & Seze, G. (1994). The
492 POLDER mission: instrument characteristics and scientific objectives. *Ieee Transactions on Geoscience
493 and Remote Sensing*, 32, 598-615, doi:10.1109/36.297978
- 494 Deuzé, J.L., Bréon, F.M., Devaux, C., Goloub, P., Herman, M., Lafrance, B., Maignan, F., Marchand, A.,
495 Nadal, F., Perry, G., & Tanré, D. (2001). Remote sensing of aerosols over land surfaces from POLDER-
496 ADEOS-1 polarized measurements. *Journal of Geophysical Research: Atmospheres*, 106, 4913-4926,
497 doi:10.1029/2000jd900364
- 498 Diner, D.J., Beckert, J.C., Reilly, T.H., Bruegge, C.J., Conel, J.E., Kahn, R.A., Martonchik, J.V.,

499 Ackerman, T.P., Davies, R., Gerstl, S.A.W., Gordon, H.R., Muller, J.P., Myneni, R.B., Sellers, P.J., Pinty,
500 B., & Verstraete, M.M. (1998). Multi-angle Imaging SpectroRadiometer (MISR) - Instrument description
501 and experiment overview. *Ieee Transactions on Geoscience and Remote Sensing*, *36*, 1072-1087,
502 doi:10.1109/36.700992

503 Dubovik, O., Fuertes, D., Litvinov, P., Lopatin, A., Lapyonok, T., Dubovik, I., Xu, F., Ducos, F., Chen,
504 C., Torres, B., Derimian, Y., Li, L., Herreras-Giralda, M., Herrera, M., Karol, Y., Matar, C., Schuster,
505 G.L., Espinosa, R., Puthukkudy, A., Li, Z., Fischer, J., Preusker, R., Cuesta, J., Kreuter, A., Cede, A.,
506 Aspetsberger, M., Marth, D., Bindreiter, L., Hangler, A., Lanzinger, V., Holter, C., & Federspiel, C.
507 (2021). A Comprehensive Description of Multi-Term LSM for Applying Multiple a Priori Constraints in
508 Problems of Atmospheric Remote Sensing: GRASP Algorithm, Concept, and Applications. *Frontiers in*
509 *Remote Sensing*, *2*:706851, doi:10.3389/frsen.2021.706851

510 Dubovik, O., Herman, M., Holdak, A., Lapyonok, T., Tanre, D., Deuze, J.L., Ducos, F., Sinyuk, A., &
511 Lopatin, A. (2011). Statistically optimized inversion algorithm for enhanced retrieval of aerosol
512 properties from spectral multi-angle polarimetric satellite observations. *Atmospheric Measurement*
513 *Techniques*, *4*, 975-1018, doi:10.5194/amt-4-975-2011

514 Dubovik, O., & King, M.D. (2000). A flexible inversion algorithm for retrieval of aerosol optical
515 properties from Sun and sky radiance measurements. *Journal of Geophysical Research Atmospheres*, *105*,
516 20673-20696, doi:10.1029/2000JD900282

517 Dubovik, O., Lapyonok, T., Litvinov, P., Herman, M., Fuertes, D., Ducos, F., Lopatin, A., Chaikovsky,
518 A., Torres, B., Derimian, Y., Huang, X., Aspetsberger, M., & Federspiel, C. (2014). GRASP: a versatile
519 algorithm for characterizing the atmosphere. *SPIE Newsroom*, doi:10.1117/2.1201408.005558

520 Dubovik, O., Li, Z., Mishchenko, M.I., Tanré, D., Karol, Y., Bojkov, B., Cairns, B., Diner, D.J., Espinosa,
521 W.R., Goloub, P., Gu, X., Hasekamp, O., Hong, J., Hou, W., Knobelspiesse, K.D., Landgraf, J., Li, L.,
522 Litvinov, P., Liu, Y., Lopatin, A., Marbach, T., Maring, H., Martins, V., Meijer, Y., Milinevsky, G., Mukai,
523 S., Parol, F., Qiao, Y., Remer, L., Rietjens, J., Sano, I., Stammes, P., Stammes, S., Sun, X., Tabary, P.,
524 Travis, L.D., Waquet, F., Xu, F., Yan, C., & Yin, D. (2019). Polarimetric remote sensing of atmospheric
525 aerosols: Instruments, methodologies, results, and perspectives. *Journal of Quantitative Spectroscopy*
526 *and Radiative Transfer*, *224*, 474-511, doi:10.1016/j.jqsrt.2018.11.024

527 Dubovik, O., Sinyuk, A., Lapyonok, T., Holben, B.N., Mishchenko, M., Yang, P., Eck, T.F., Volten, H.,
528 Munoz, O., Veihelmann, B., van der Zande, W.J., Leon, J.F., Sorokin, M., & Slutsker, I. (2006).
529 Application of spheroid models to account for aerosol particle nonsphericity in remote sensing of desert
530 dust. *Journal of Geophysical Research-Atmospheres*, *111*, D11208, doi:10.1029/2005jd006619

531 Eck, T.F., Holben, B.N., Reid, J.S., Dubovik, O., Smirnov, A., O'Neill, N.T., Slutsker, I., & Kinne, S.
532 (1999). Wavelength dependence of the optical depth of biomass burning, urban, and desert dust aerosols.
533 *Journal of Geophysical Research: Atmospheres*, *104*, 31333-31349, doi:10.1029/1999jd900923

534 Eck, T.F., Holben, B.N., Sinyuk, A., Pinker, R.T., Goloub, P., Chen, H., Chatenet, B., Li, Z., Singh, R.P.,
535 Tripathi, S.N., Reid, J.S., Giles, D.M., Dubovik, O., O'Neill, N.T., Smirnov, A., Wang, P., & Xia, X.
536 (2010). Climatological aspects of the optical properties of fine/coarse mode aerosol mixtures. *Journal of*
537 *Geophysical Research*, *115*, D19205, doi:10.1029/2010jd014002

538 Gao, J., Woodward, A., Vardoulakis, S., Kovats, S., Wilkinson, P., Li, L., Xu, L., Li, J., Yang, J., Li, J.,
539 Cao, L., Liu, X., Wu, H., & Liu, Q. (2017). Haze, public health and mitigation measures in China: A
540 review of the current evidence for further policy response. *Science of the Total Environment*, *578*, 148-
541 157, doi:<https://doi.org/10.1016/j.scitotenv.2016.10.231>

542 Ge, B., Mei, X., Li, Z., Hou, W., Xie, Y., Zhang, Y., Xu, H., Li, K., & Wei, Y. (2020). An improved

543 algorithm for retrieving high resolution fine-mode aerosol based on polarized satellite data: Application
544 and validation for POLDER-3. *Remote Sensing of Environment*, 247, 111894,
545 doi:10.1016/j.rse.2020.111894

546 Goloub, P., & Deuze, J.L. (1994). Analysis of the POLDER polarization measurements performed over
547 cloud covers. *IEEE Transactions on Geoscience & Remote Sensing*, 32, 78-88, doi:10.1109/36.285191

548 Gomez-Chova, L., Camps-Valls, G., Calpe-Maravilla, J., Guanter, L., & Moreno, J. (2007). Cloud-
549 screening algorithm for ENVISAT/MERIS multispectral images. *Ieee Transactions on Geoscience and*
550 *Remote Sensing*, 45, 4105-4118, doi:10.1109/tgrs.2007.905312

551 Guo, J., Deng, M., Lee, S.S., Wang, F., Li, Z., Zhai, P., Liu, H., Lv, W., Yao, W., & Li, X. (2016). Delaying
552 precipitation and lightning by air pollution over the Pearl River Delta. Part I: Observational analyses.
553 *Journal of Geophysical Research: Atmospheres*, 121, 6472-6488, doi:10.1002/2015jd023257

554 Gupta, P., Remer, L.A., Levy, R.C., & Mattoo, S. (2018). Validation of MODIS 3 km land aerosol optical
555 depth from NASA's EOS Terra and Aqua missions. *Atmospheric Measurement Techniques*, 11, 3145-
556 3159, doi:10.5194/amt-11-3145-2018

557 Hagolle, O., Goloub, P., Deschamps, P.-Y., Cosnefroy, H., Briottet, X., Bailleul, T., Nicolas, J.-M., Parol,
558 F., Lafrance, B., & Herman, M. (1999). Results of POLDER in-flight calibration. *Ieee Transactions on*
559 *Geoscience and Remote Sensing*, 37, 1550-1566, doi:10.1109/36.763266

560 Holben, B.N., Eck, T.F., Slutsker, I., Tanre, D., Buis, J.P., Setzer, A., Vermote, E., Reagan, J.A., Kaufman,
561 Y.J., Nakajima, T., Lavenu, F., Jankowiak, I., & Smirnov, A. (1998). AERONET - A federated instrument
562 network and data archive for aerosol characterization. *Remote Sensing of Environment*, 66, 1-16,
563 doi:10.1016/s0034-4257(98)00031-5

564 Hsu, N.C., Jeong, M.J., Bettenhausen, C., Sayer, A.M., Hansell, R., Seftor, C.S., Huang, J., & Tsay, S.C.
565 (2013). Enhanced Deep Blue aerosol retrieval algorithm: The second generation. *Journal of Geophysical*
566 *Research: Atmospheres*, 118, 9296-9315, doi:10.1002/jgrd.50712

567 Hsu, N.C., Tsay, S.C., King, M.D., & Herman, J.R. (2004). Aerosol properties over bright-reflecting
568 source regions. *IEEE Transactions on Geoscience & Remote Sensing*, 42, 557-569,
569 doi:10.1109/TGRS.2004.824067

570 Jin, S., Ma, Y., Zhang, M., Gong, W., Dubovik, O., Liu, B., Shi, Y., & Yang, C. (2019). Retrieval of 500
571 m Aerosol Optical Depths from MODIS Measurements over Urban Surfaces under Heavy Aerosol
572 Loading Conditions in Winter. *Remote Sensing*, 11, 2218, doi:10.3390/rs11192218

573 Jin, S., Zhang, M., Ma, Y., Gong, W., Chen, C., Yang, L., Hu, X., Liu, B., Chen, N., Du, B., & Shi, Y.
574 (2021). Adapting the Dark Target Algorithm to Advanced MERSI Sensor on the FengYun-3-D Satellite:
575 Retrieval and Validation of Aerosol Optical Depth Over Land. *Ieee Transactions on Geoscience and*
576 *Remote Sensing*, 59, 8781-8797, doi:10.1109/TGRS.2020.3021021

577 Kacenelenbogen, M., Leon, J.F., Chiapello, I., & Tanre, D. (2006). Characterization of aerosol pollution
578 events in France using ground-based and POLDER-2 satellite data. *Atmospheric Chemistry and Physics*,
579 6, 4843-4849, doi:10.5194/acp-6-4843-2006

580 Kaufman, Y.J., Tanré, D., Gordon, H.R., Nakajima, T., Lenoble, J., Frouin, R., Grassl, H., Herman, B.M.,
581 King, M.D., & Teillet, P.M. (1997). Passive remote sensing of tropospheric aerosol and atmospheric
582 correction for the aerosol effect. *Journal of Geophysical Research: Atmospheres*, 102, 16815-16830,
583 doi:10.1029/97jd01496

584 Koren, I., Remer, L.A., Kaufman, Y.J., Rudich, Y., & Martins, J.V. (2007). On the twilight zone between
585 clouds and aerosols. *Geophysical Research Letters*, 34, L08805, doi:10.1029/2007gl029253

586 Lenoble, J., Remer, L., & Tanre, D. (2013). *Aerosol Remote Sensing*. Springer-Verlag Berlin Heidelberg,

587 doi:10.1007/978-3-642-17725-5

588 Levy, R.C., Mattoo, S., Munchak, L.A., Remer, L.A., Sayer, A.M., Patadia, F., & Hsu, N.C. (2013). The
589 Collection 6 MODIS aerosol products over land and ocean. *Atmospheric Measurement Techniques*, 6,
590 2989-3034, doi:10.5194/amt-6-2989-2013

591 Li, J.H., Ma, J.J., Li, C., Wang, Y.Y., Li, Z.Q., & Hong, J. (2021). Multi-information collaborative cloud
592 identification algorithm in Gaofen-5 Directional Polarimetric Camera imagery. *Journal of Quantitative
593 Spectroscopy & Radiative Transfer*, 261, 107439, doi:10.1016/j.jqsrt.2020.107439

594 Li, L., Che, H., Zhang, X., Chen, C., Chen, X., Gui, K., Liang, Y., Wang, F., Derimian, Y., Fuertes, D.,
595 Dubovik, O., Zheng, Y., Zhang, L., Guo, B., Wang, Y., & Zhang, X. (2022). A satellite-measured view of
596 aerosol component content and optical property in a haze-polluted case over North China Plain.
597 *Atmospheric Research*, 266, 105958, doi:<https://doi.org/10.1016/j.atmosres.2021.105958>

598 Li, L., Dubovik, O., Derimian, Y., Schuster, G.L., Lapyonok, T., Litvinov, P., Ducos, F., Fuertes, D., Chen,
599 C., Li, Z., Lopatin, A., Torres, B., & Che, H. (2019). Retrieval of aerosol components directly from
600 satellite and ground-based measurements. *Atmospheric Chemistry and Physics*, 19, 13409-13443,
601 doi:10.5194/acp-19-13409-2019

602 Li, X., & Strahler, A.H. (1992). Geometric-optical bidirectional reflectance modeling of the discrete
603 crown vegetation canopy: effect of crown shape and mutual shadowing. *Ieee Transactions on Geoscience
604 and Remote Sensing*, 30, 276-292, doi:10.1109/36.134078

605 Li, Z., Hou, W., Hong, J., Zheng, F., Luo, D., Wang, J., Gu, X., & Qiao, Y. (2018). Directional
606 Polarimetric Camera (DPC): Monitoring aerosol spectral optical properties over land from satellite
607 observation. *Journal of Quantitative Spectroscopy and Radiative Transfer*, 218, 21-37,
608 doi:10.1016/j.jqsrt.2018.07.003

609 Li, Z.Q., Lau, W.K.M., Ramanathan, V., Wu, G., Ding, Y., Manoj, M.G., Liu, J., Qian, Y., Li, J., Zhou,
610 T., Fan, J., Rosenfeld, D., Ming, Y., Wang, Y., Huang, J., Wang, B., Xu, X., Lee, S.S., Cribb, M., Zhang,
611 F., Yang, X., Zhao, C., Takemura, T., Wang, K., Xia, X., Yin, Y., Zhang, H., Guo, J., Zhai, P.M., Sugimoto,
612 N., Babu, S.S., & Brasseur, G.P. (2016). Aerosol and monsoon climate interactions over Asia. *Reviews
613 of Geophysics*, 54, 866-929, doi:10.1002/2015rg000500

614 Liu, B., Ma, X., Ma, Y., Li, H., Jin, S., Fan, R., & Gong, W. (2022). The relationship between atmospheric
615 boundary layer and temperature inversion layer and their aerosol capture capabilities. *Atmospheric
616 Research*, 271, 106121, doi:10.1016/j.atmosres.2022.106121

617 Lopatin, A., Dubovik, O., Fuertes, D., Stenchikov, G., Lapyonok, T., Veselovskii, I., Wienhold, F.G.,
618 Shevchenko, I., Hu, Q., & Parajuli, S. (2021). Synergy processing of diverse ground-based remote
619 sensing and in situ data using the GRASP algorithm: applications to radiometer, lidar and radiosonde
620 observations. *Atmos. Meas. Tech.*, 14, 2575-2614, doi:10.5194/amt-14-2575-2021

621 Lyapustin, A., Wang, Y., Korokin, S., & Dong, H. (2018). MODIS Collection 6 MAIAC algorithm.
622 *Atmospheric Measurement Techniques*, 11, 5741-5765, doi:10.5194/amt-11-5741-2018

623 Ma, Y., Zhu, Y., Liu, B., Li, H., Jin, S., Zhang, Y., Fan, R., & Gong, W. (2021). Estimation of the vertical
624 distribution of particle matter (PM_{2.5}) concentration and its transport flux from lidar measurements
625 based on machine learning algorithms. *Atmospheric Chemistry and Physics*, 21, 17003-17016,
626 doi:10.5194/acp-21-17003-2021

627 Martins, J.V., Tanré, D., Remer, L., Kaufman, Y., Mattoo, S., & Levy, R. (2002). MODIS Cloud screening
628 for remote sensing of aerosols over oceans using spatial variability. *Geophysical Research Letters*, 29,
629 MOD4, doi:10.1029/2001GL013252

630 McCormick, M.P., Hamill, P., Pepin, T.J., Chu, W.P., Swissler, T.J., & McMaster, L.R. (1979).

631 SATELLITE STUDIES OF THE STRATOSPHERIC AEROSOL. *Bulletin of the American*
632 *Meteorological Society*, 60, 1038-1046, doi:10.1175/1520-0477(1979)060<1038:ssotsa>2.0.co;2

633 Mishchenko, M.I., & Travis, L.D. (1997). Satellite retrieval of aerosol properties over the ocean using
634 polarization as well as intensity of reflected sunlight. *Journal of Geophysical Research: Atmospheres*,
635 102, 16989-17013, doi:<https://doi.org/10.1029/96JD02425>

636 Nadal, F., & Bréon, F.M. (1999). Parameterization of Surface Polarized Reflectance Derived from
637 POLDER Spaceborne Measurements. *IEEE Transactions on Geoscience & Remote Sensing*, 37, 1709-
638 1718, doi:10.1109/36.763292

639 Nakajima, T., Yoon, S.C., Ramanathan, V., Shi, G.Y., Takemura, T., Higurashi, A., Takamura, T., Aoki,
640 K., Sohn, B.J., Kim, S.W., Tsuruta, H., Sugimoto, N., Shimizu, A., Tanimoto, H., Sawa, Y., Lin, N.H.,
641 Lee, C.T., Goto, D., & Schutgens, N. (2007). Overview of the Atmospheric Brown Cloud East Asian
642 Regional Experiment 2005 and a study of the aerosol direct radiative forcing in east Asia. *Journal of*
643 *Geophysical Research-Atmospheres*, 112, 23, doi:10.1029/2007jd009009

644 Ou, Y., Li, L., Ying, Z., Dubovik, O., Derimian, Y., Chen, C., Fuertes, D., Xie, Y., Lopatin, A., Ducos, F.,
645 & Peng, Z. (2021). Spatio-Temporal Variability of Aerosol Components, Their Optical and
646 Microphysical Properties over North China during Winter Haze in 2012, as Derived from
647 POLDER/PARASOL Satellite Observations. *Remote Sensing*, 13, 2682, doi:10.3390/rs13142682

648 Qie, L., Li, Z., Zhu, S., Xu, H., Xie, Y., Qiao, R., Hong, J., & Tu, B. (2021). In-flight radiometric and
649 polarimetric calibration of the Directional Polarimetric Camera onboard the GaoFen-5 satellite over the
650 ocean. *Appl Opt*, 60, 7186-7199, doi:10.1364/AO.422980

651 Rao, C.R.N., Stowe, L.L., & McClain, E.P. (1989). REMOTE-SENSING OF AEROSOLS OVER THE
652 OCEANS USING AVHRR DATA THEORY, PRACTICE AND APPLICATIONS. *International Journal*
653 *of Remote Sensing*, 10, 743-749, doi:10.1080/01431168908903915

654 Remer, L.A., Mattoo, S., Levy, R.C., Heidinger, A., Pierce, R.B., & Chin, M. (2012). Retrieving aerosol
655 in a cloudy environment: aerosol product availability as a function of spatial resolution. *Atmospheric*
656 *Measurement Techniques*, 5, 1823-1840, doi:10.5194/amt-5-1823-2012

657 Rosenfeld, D., Lohmann, U., Raga, G.B., O'Dowd, C.D., Kulmala, M., Fuzzi, S., Reissell, A., & Andreae,
658 M.O. (2008). Flood or drought: How do aerosols affect precipitation? *Science*, 321, 1309-1313,
659 doi:10.1126/science.1160606

660 Sayer, A.M., Hsu, N.C., Bettenhausen, C., & Jeong, M.J. (2013). Validation and uncertainty estimates
661 for MODIS Collection 6 "Deep Blue" aerosol data. *Journal of Geophysical Research: Atmospheres*, 118,
662 7864-7872, doi:10.1002/jgrd.50600

663 Sayer, A.M., Munchak, L.A., Hsu, N.C., Levy, R.C., Bettenhausen, C., & Jeong, M.J. (2014). MODIS
664 Collection 6 aerosol products: Comparison between Aqua's e-Deep Blue, Dark Target, and "merged" data
665 sets, and usage recommendations. *Journal of Geophysical Research-Atmospheres*, 119, 13965-13989,
666 doi:10.1002/2014jd022453

667 Shi, T., Han, G., Ma, X., Gong, W., Chen, W., Liu, J., Zhang, X., Pei, Z., Gou, H., & Bu, L. (2021).
668 Quantifying CO₂ Uptakes Over Oceans Using LIDAR: A Tentative Experiment in Bohai Bay.
669 *Geophysical Research Letters*, 48, e2020GL091160, doi:<https://doi.org/10.1029/2020GL091160>

670 Tanre, D., Breon, F.M., Deuze, J.L., Dubovik, O., Ducos, F., Francois, P., Goloub, P., Herman, M.,
671 Lifermann, A., & Waquet, F. (2011). Remote sensing of aerosols by using polarized, directional and
672 spectral measurements within the A-Train: the PARASOL mission. *Atmospheric Measurement*
673 *Techniques*, 4, 1383-1395, doi:10.5194/amt-4-1383-2011

674 Tegen, I., & Lacis, A.A. (1996). Modeling of particle size distribution and its influence on the radiative

675 properties of mineral dust aerosol. *Journal of Geophysical Research Atmospheres*, 101, 19237-19244,
 676 doi:10.1029/95JD03610

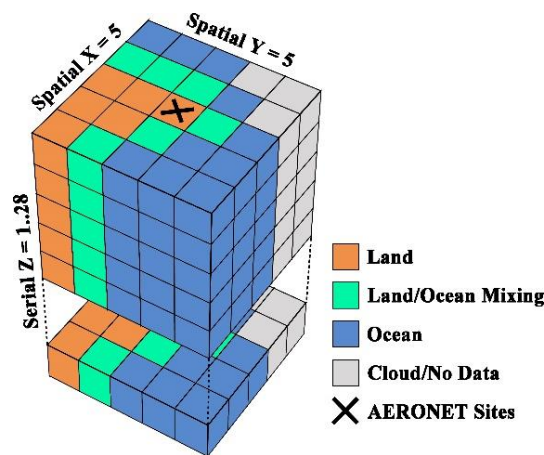
677 Zhang, M., Jin, S., Ma, Y., Fan, R., Wang, L., Gong, W., & Liu, B. (2021). Haze events at different levels
 678 in winters: A comprehensive study of meteorological factors, Aerosol characteristics and direct radiative
 679 forcing in megacities of north and central China. *Atmospheric Environment*, 245, 118056,
 680 doi:<https://doi.org/10.1016/j.atmosenv.2020.118056>

681 Zhdanova, E.Y., Chubarova, N.Y., & Lyapustin, A.I. (2020). Assessment of urban aerosol pollution over
 682 the Moscow megacity by the MAIAC aerosol product. *Atmospheric Measurement Techniques*, 13, 877-
 683 891, doi:10.5194/amt-13-877-2020

684 Zhu, S., Li, Z., Qie, L., Xu, H., Ge, B., Xie, Y., Qiao, R., Xie, Y., Hong, J., Meng, B., Tu, B., & Chen, F.
 685 (2022). In-Flight Relative Radiometric Calibration of a Wide Field of View Directional Polarimetric
 686 Camera Based on the Rayleigh Scattering over Ocean. *Remote Sensing*, 14, doi:10.3390/rs14051211

687 Zhu, Z., & Woodcock, C.E. (2012). Object-based cloud and cloud shadow detection in Landsat imagery.
 688 *Remote Sensing of Environment*, 118, 83-94, doi:10.1016/j.rse.2011.10.028

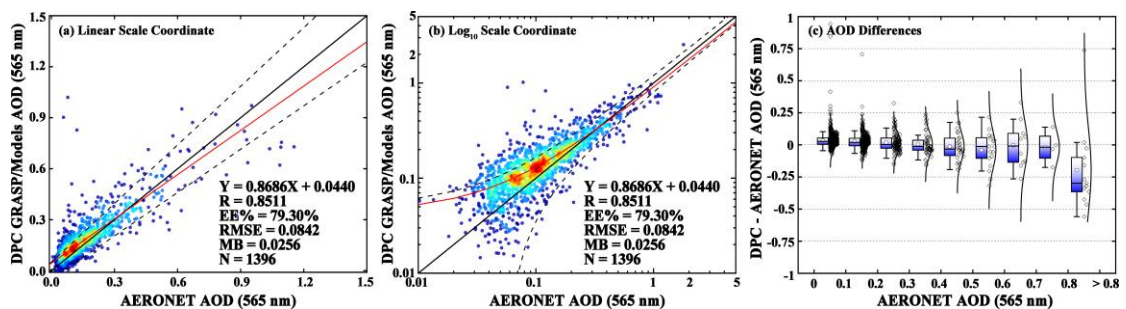
689



690

691 **Figure 1.** Schematic diagram for multi-pixel retrieval unit ($5 \times 5 \times 1..28$). A maximum of 28 sequences
 692 allowed in each unit is limited by hardware memory.

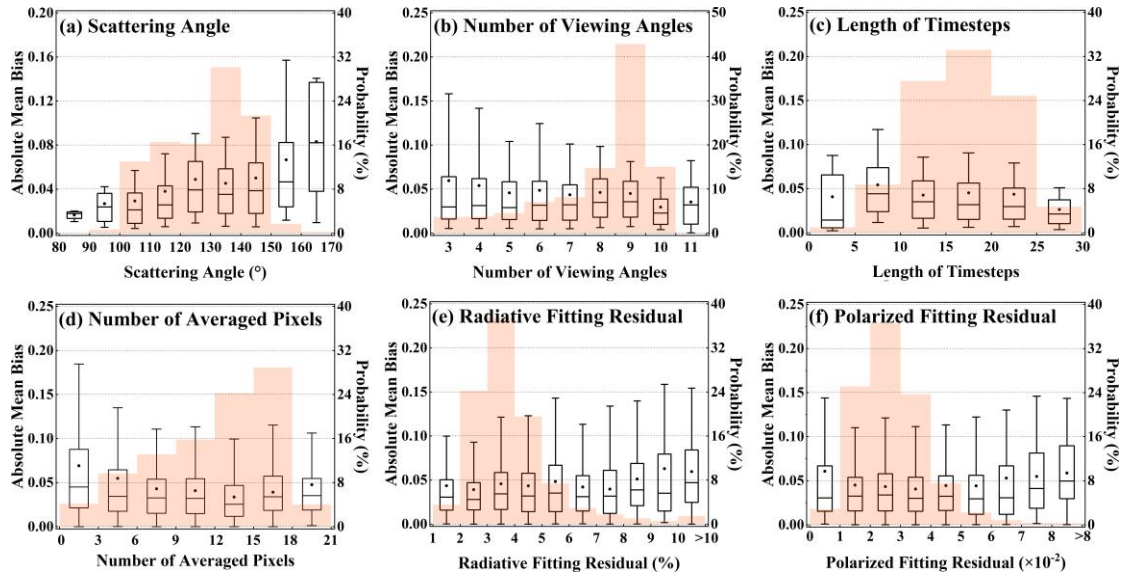
693



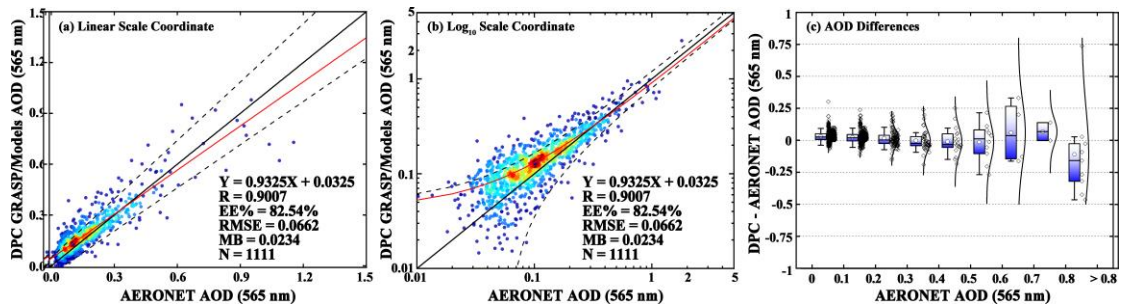
694

695 **Figure 2.** (a) Density scatterplot of AOD retrievals from DPC with the GRASP/Models scheme
 696 versus the AERONET observations with a linear coordinate system. (b) The density scatterplot with
 697 a logarithmic coordinate system. The solid black line is the one to one and the dashed black lines
 698 show the ranges of Expected Error. The red solid lines represent the linear regression line; (c) Box
 699 plots show changes of differences between DPC GRASP/Models and AEROENT with AOD
 700 increasing. Diamond marks and curves represent distributions of sample and normal distribution

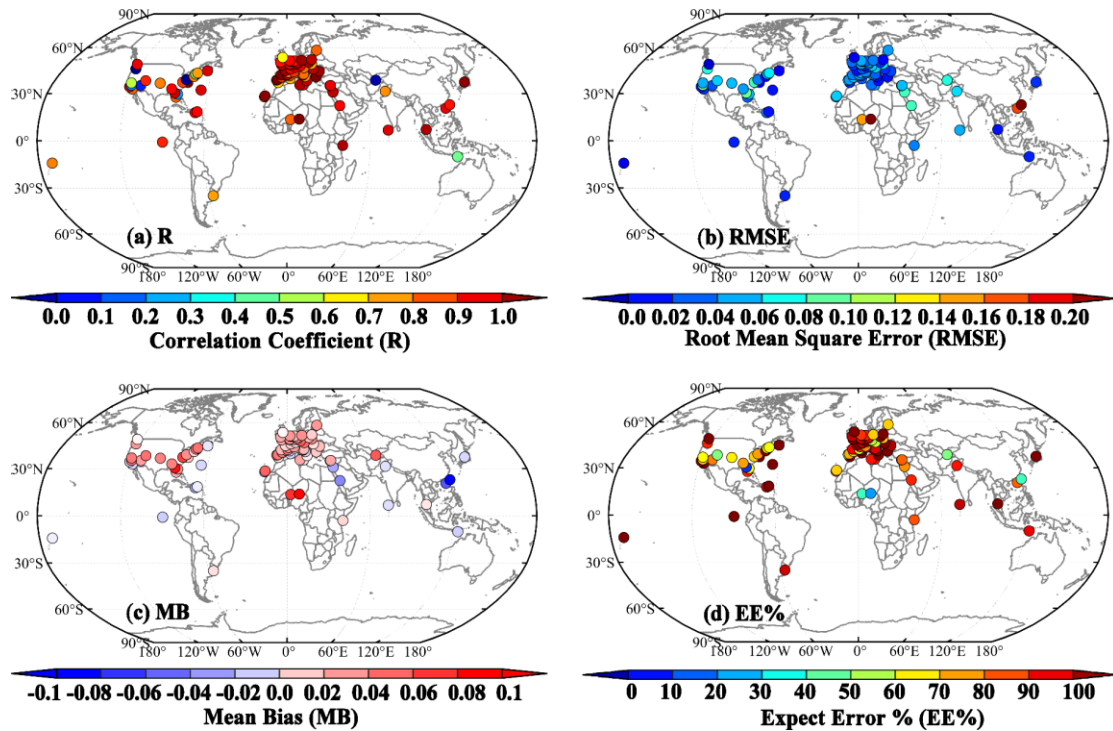
701 fitting lines, respectively.
 702



703
 704 **Figure 3.** Influencing factors of AOD retrieval performance of DPC based on the GRASP/Models:
 705 (a) SCA; (b) number of viewing angles; (c) length of timesteps; (d) number of averaged pixels; (e)
 706 non-polarized fitting residual; (f) polarized fitting residual. Orange shadows in the background
 707 represents the probability distribution of the samples.
 708

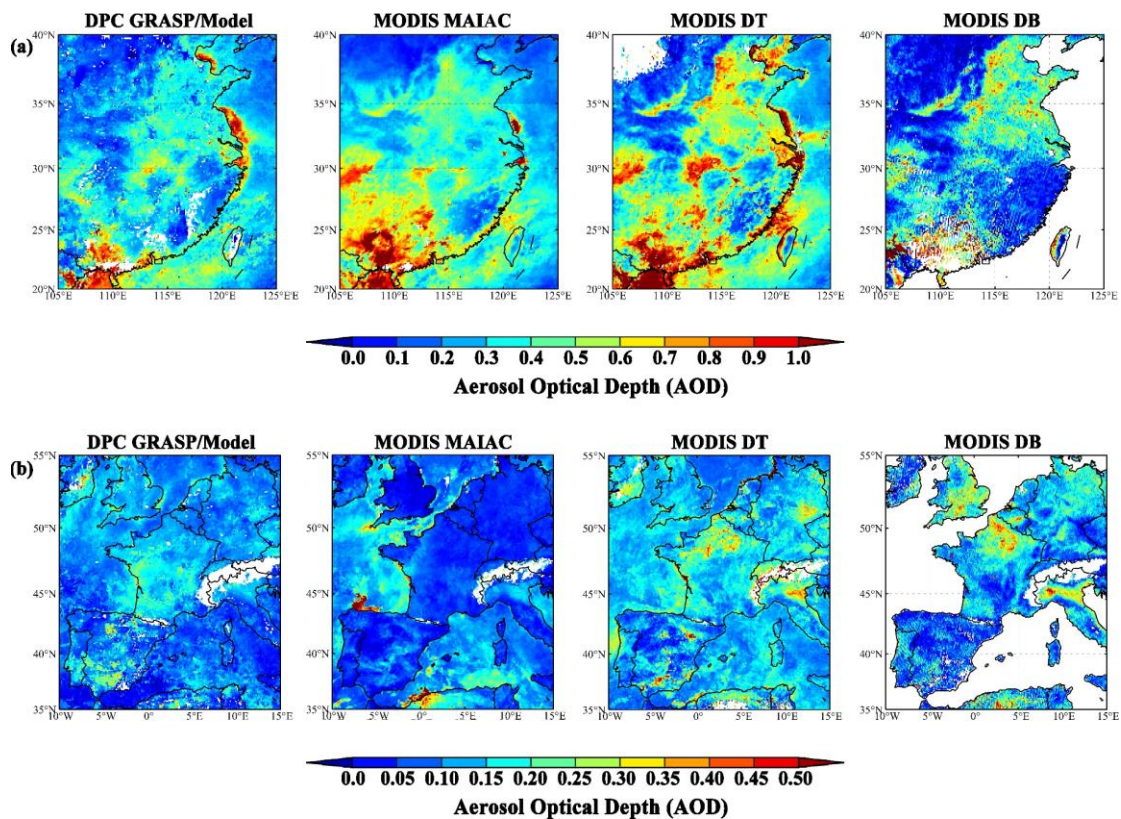


709
 710 **Figure 4.** (a) Density scatterplot of AOD retrievals from DPC with the GRASP/Models scheme
 711 versus the AERONET observations with a logarithmic coordinate system after quality control. (b)
 712 The density scatterplot with a logarithmic coordinate system. The solid black lines are diagonal and
 713 the dashed black lines show the ranges of Expected Error. The red solid lines represent the linear
 714 regression line; (c) Box plots show changes of differences between DPC GRASP/Models and
 715 AEROENT with AOD increasing. Diamond marks and curves represent distributions of sample and
 716 normal distribution fitting lines, respectively.
 717
 718



719
720
721
722
723

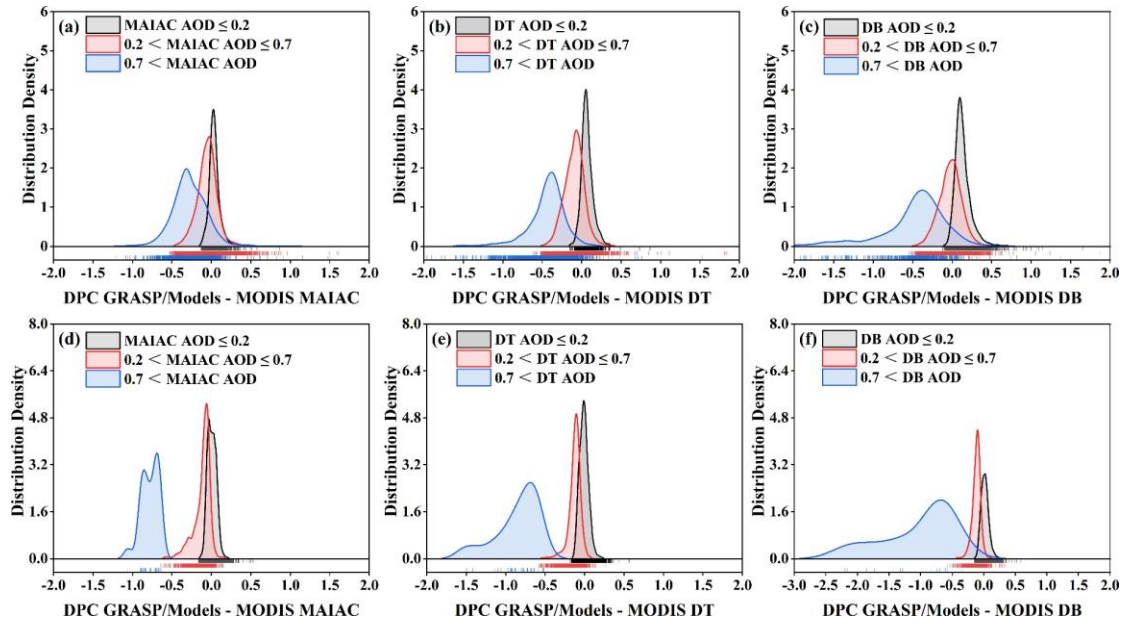
Figure 5. Spatial Distributions of (a) R, (b) RMSE, (c) MB, and (d) EE% calculated from DPC GRASP/Models by compared with AERONET observations. Only sites with more than 5 matching points are included.



724
725
726

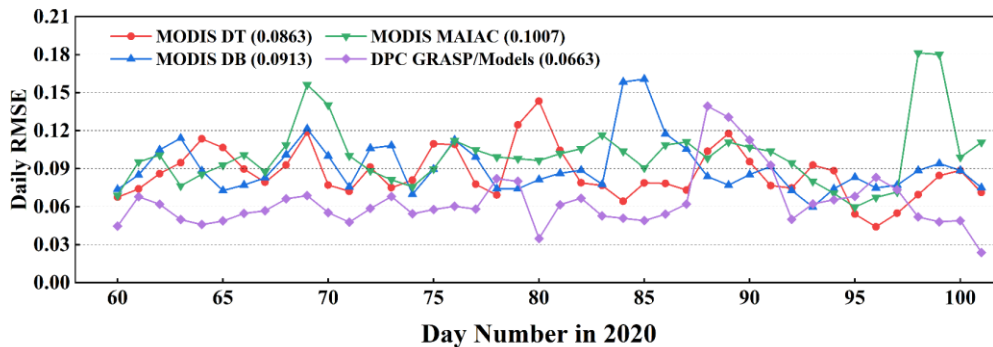
Figure 6. Spatial distribution of AOD from DPC GRASP/Models compared with MODIS MAIMC, DT, and DB aerosol products in March, 2020: (a) Eastern and Southern China with its adjacent sea

727 areas; (b) Areas of Western Europe including the Atlantic Ocean and the Mediterranean. The DPC
 728 AOD is at 565 nm and the MODIS AOD is at 550 nm.
 729



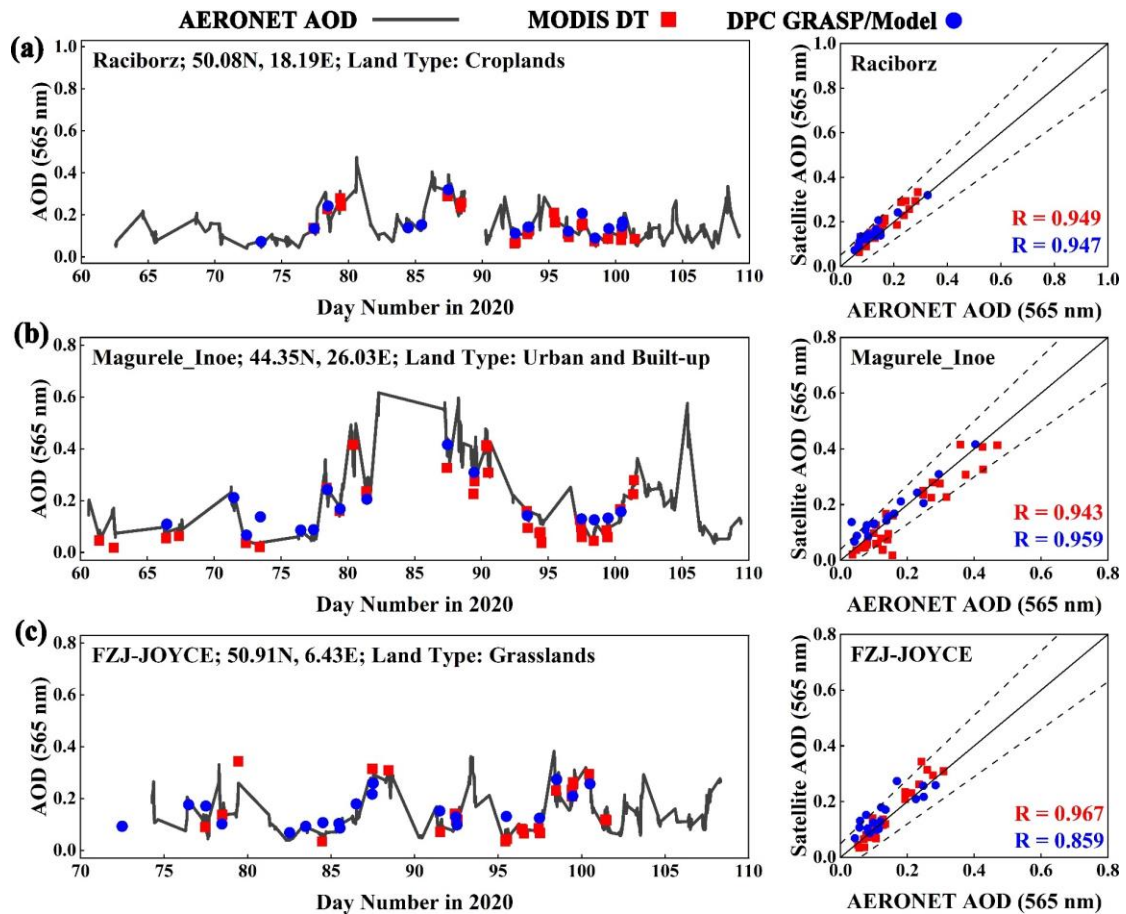
730
 731 **Figure 7.** Distribution Density of AOD differences between DPC GRASP/Models and MODIS DT,
 732 DB, and MAIAC products at: (a-c) Eastern and Southern China with its adjacent sea areas; (d-e)
 733 Areas of Western Europe including the Atlantic Ocean and the Mediterranean. It is noted that the
 734 MODIS DB product only releases terrestrial AOD data.

735
 736



737
 738 **Figure 8.** Time series of daily RMSE for the selected AERONET stations during March and April
 739 of 2020. The number in brackets are averaged values of daily RMSE. The positions of AERONET
 740 stations are the same with **Figure 5**.

741



742

743

Figure 9. Time series of AOD from the DPC GRASP/Models versus the MODIS DT products and AERONET observations at three sites as cases: (a) Raciborz, (b) Magurele_Inoe, and (c) FZJ-JOYCE. The scatterplot shows the relationship between AERONET AOD and satellite AOD.

744

745

746